Temperature Dependence of the Energy Levels of Methylammonium Lead Iodide Perovskite from First Principles

Wissam A. Saidi,[1,*] Samuel Poncé,[2] and Bartomeu Monserrat[3,4]

[1] *Department of Mechanical Engineering and Materials Science, University of Pittsburgh, Pittsburgh 15261, USA*
[2] *Department of Materials, University of Oxford, Parks Road, Oxford OX1 3PH, United Kingdom*
[3] *Department of Physics and Astronomy, Rutgers University, Piscataway, New Jersey 08854-8019, USA*
[4] *TCM Group, Cavendish Laboratory, University of Cambridge, J. J. Thomson Avenue, Cambridge CB3 0HE, United Kingdom*

(Dated: December 5, 2016)

Environmental effects and intrinsic energy-loss processes lead to fluctuations in the operational temperature of solar cells, which can profoundly influence their power conversion efficiency. Here we determine from first principles the effects of temperature on the band gap and band edges of the hybrid pervoskite $CH_3NH_3PbI_3$ by accounting for electron-phonon coupling and thermal expansion. From 290 to 380 K, the computed band gap change of 40 meV coincides with the experimental change of 30-40 meV. The calculation of electron-phonon coupling in $CH_3NH_3PbI_3$ is particularly intricate, as the commonly used Allen-Heine-Cardona theory overestimates the band gap change with temperature, and excellent agreement with experiment is only obtained when including high-order terms in the electron-phonon interaction. We also find that spin-orbit coupling enhances the electron-phonon coupling strength, but that the inclusion of nonlocal correlations using hybrid functionals has little effect. We reach similar conclusions in the metal-halide perovskite $CsPbI_3$. Our results unambiguously confirm for the first time the importance of high-order terms in the electron-phonon coupling by direct comparison with experiment.

Metal-halide hybrid perovskites are promising candidates as light absorbers for the next generation of solid state hybrid photovoltaic devices [1–7]. Their solar power conversion efficiency has reached 22.1% [8], an impressive achievement considering that the first perovskite-based solar cell was only made seven years ago [1]. These light-absorbing materials belong to the perovskite family ABX_3, where A is a cation located at the center of a cube formed from corner-sharing BX_6 octahedra.

Methylammonium lead iodide $MAPbI_3$, where MA represents the organic cation $CH_3NH_3^+$, has an optimal band gap for light absorption of 1.6 eV and exhibits large electron and hole diffusion lengths, which make it a prime candidate for solar cell applications [3, 4]. Another factor determining the efficiency of a solar cell is the band alignment between the light absorber and its transport layers [9]. As an example, a common electron transport layer is TiO_2, which has a conduction band that is only 0.1 eV lower than that of $MAPbI_3$ [10].

Solar cell devices are subject to significant temperature variations under normal operating conditions [11]. Ambient temperatures can oscillate between 250 and 310 K, and energy-loss mechanisms associated with the conversion of solar power to electric power can increase the operating temperature of the cell above 340 K [11–13]. These temperature fluctuations can affect both the absorption onset and band alignment, and therefore the performance of the solar cell, as was demonstrated for $MAPbI_3$-based solar cells, which showed an open circuit voltage drop from 1.01 V to 0.83 V as temperature increased from 300 to 360 K [14]. Recently, two experimental studies have investigated the temperature-dependent properties of $MAPbI_3$ and reported changes in the band gap reaching 40 meV in the temperature range of solar cell operation [15, 16], and even larger changes exceeding 100 meV in the individual band edges [15].

While the properties of $MAPbI_3$ are well-characterized both theoretically and experimentally, there is an increasing research effort to find alternatives to this light absorber [17–20]. with the aim of tuning the physical properties of the solar cells and moving towards lead-free devices. In this context, it would be desirable to accurately calculate the effects of temperature changes to aid in the computational design of novel perovskite solar cell materials under real working conditions. Unfortunately, the organic-inorganic nature of $MAPbI_3$, together with the presence of the heavy Pb atoms, make it a challenging system to study from first principles [21–28].

In this Letter, we determine the temperature evolution of the band gap and band edges in $MAPbI_3$ using first-principles methods while accounting for both electron-phonon coupling and thermal expansion. Our results accurately reproduce the band gap opening observed experimentally in $MAPbI_3$ upon increasing temperature [15, 16]. We further show that the commonly used Allen-Heine-Cardona (AHC) theory [29, 30], which successfully captures the low-order terms in electron-phonon coupling and can be used to explain the temperature dependence of band gaps in multiple systems, fails in $MAPbI_3$ because high-order terms in the electron-phonon interaction make significant contributions. Furthermore, we show that spin-orbit coupling (SOC) must be included to accurately describe the electron-phonon coupling strength of this system, while nonlocal corre-

lation effects incorporated using a hybrid functional do not yield significant changes. Our final results are in excellent agreement with experimental data, thus verifying that thermal effects can be reliably computed using first-principles methods to design novel perovskite solar cells. Additionally, our demonstration that a low-order treatment of the electron-phonon interactions fails for the band edges of perovskite solar cell materials raises the question of whether this would also be true for other electronic states in the Brillouin zone. Quantities such as electronic transport depend on the electron-phonon interaction averaged over the entire Brillouin zone, and therefore it would be interesting to study whether the standard approach to these calculations based on a low-order treatment of electron-phonon coupling is valid.

Methodology. Our calculations are based on density functional theory (DFT) [31–33] using the VASP [34–37] and ABINIT [38] software packages. We use the semi-local Perdew-Burke-Ernzerhof (PBE) [39] exchange-correlation functional, as well as the hybrid Heyd-Scuseria-Ernzerhof (HSE) [40, 41] functional, with and without SOC. The computational details are provided in the Supporting Information. To make our calculations tractable, we focus on the high temperature cubic phase of $MAPbI_3$, but we expect that our results are also applicable to the tetragonal phase that is stable below 330 K [23, 42, 43], as experimental results show that the band gap evolution with temperature transitions smoothly between the cubic and tetragonal phases [15, 16]. The cubic phase exhibits some unstable modes, and we have set their amplitudes to zero in the calculations reported. These modes can contribute to the strength of electron-phonon coupling [44], but as they represent only a small fraction of all modes, we expect their contribution to the temperature dependence of the band gap to be small. Calculations in which these modes are allowed to have nonzero amplitudes indicate that the neglect of the unstable modes leads to an error that is smaller than the statistical uncertainty in our calculations (see Supporting Information).

Allen-Heine-Cardona theory. The coupling between electronic states and nuclear vibrations due to quantum zero-point (ZP) motion and thermal motion renormalizes the electronic eigenenergies $\epsilon_{\mathbf{k}n}$ as

$$\epsilon_{\mathbf{k}n}(T) = \frac{1}{\mathcal{Z}} \sum_{\mathbf{s}} \langle \chi_{\mathbf{s}} | \epsilon_{\mathbf{k}n} | \chi_{\mathbf{s}} \rangle e^{-E_{\mathbf{s}}/k_{\mathrm{B}}T}, \qquad (1)$$

where $|\chi_{\mathbf{s}}\rangle$ is the vibrational eigenstate $\mathbf{s}$ with eigenvalue $E_{\mathbf{s}}$, $\mathcal{Z} = \sum_{\mathbf{s}} e^{-E_{\mathbf{s}}/k_{\mathrm{B}}T}$ is the partition function, T is the temperature, and k_{B} is Boltzmann constant. The evaluation of Eq. (1) is challenging, and has only recently become fully amenable to first-principles methods [45–50]. The vast majority of these calculations rely on a low-order expansion of the electronic energy as a function of the atomic displacements, leading to a particularly convenient expression for the change in the electronic energy $\Delta\epsilon_{\mathbf{k}n}(T) \triangleq \epsilon_{\mathbf{k}n}(T) - \epsilon_{\mathbf{k}n}(0)$ at temperature T:

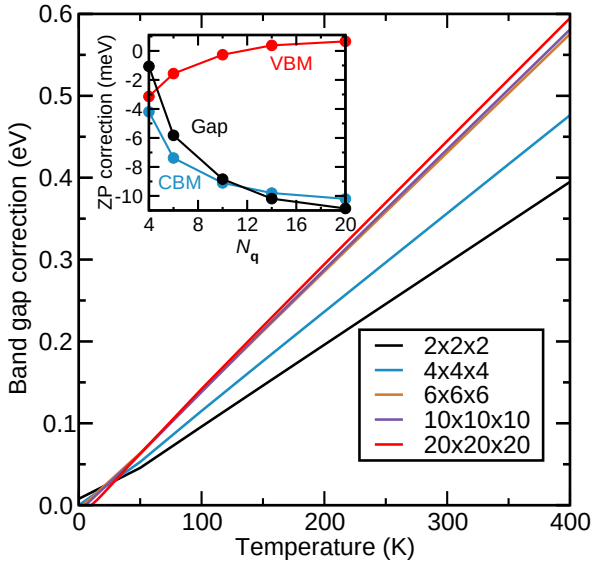

FIG. 1. Temperature dependence of the band gap of $MAPbI_3$ evaluated using the AHC approach with different BZ grids of sizes $N_{\mathbf{q}}^3$. The inset shows the convergence of the VBM, CBM and band gap ZP corrections at the $\mathbf{R}$-point as a function of the vibrational BZ grid linear size.

$$\Delta\epsilon_{\mathbf{k}n}(T) = \frac{1}{N_{\mathbf{q}}} \sum_{\mathbf{q},\nu} \frac{a^{(2)}_{\mathbf{q}\nu;\mathbf{q}\nu}}{\omega_{\mathbf{q}\nu}} \left[\frac{1}{2} + n_{\mathrm{B}}(\omega_{\mathbf{q}\nu}, T)\right], \qquad (2)$$

where $\mathbf{q}$ and ν are the phonon quantum numbers, $N_{\mathbf{q}}$ is the number of points in the vibrational Brillouin zone (BZ), $a^{(2)}_{\mathbf{q}\nu;\mathbf{q}\nu}$ is the second-order electron-phonon coupling constant, $\omega_{\mathbf{q}\nu}$ is the harmonic frequency, and n_{B} is a Bose-Einstein factor. The coupling constants can be evaluated using finite displacements (FD) in conjunction with supercells [51, 52], or using density functional perturbation theory (DFPT) by invoking the rigid-ion approximation, [53] which leads to the so-called AHC theory [29, 30]. Further details of these methods are provided in the Supporting Information.

The approximation in Eq. (2) is computationally tractable as it allows a fine sampling of the vibrational BZ because phonon modes can be treated independently. The AHC theory within DFPT can be used to sample the vibrational BZ using very fine $\mathbf{q}$-point grids, readily obtaining converged results [54]. The recent introduction of nondiagonal supercells has allowed calculations using the FD method to reach levels of convergence approaching those of DFPT [52]. In the Supporting Information we present a comparison of both approaches, which deliver similar results. We therefore infer that it is safe to apply the rigid-ion approximation in $MAPbI_3$.

Results and Discussion. We apply the AHC theory using DFPT in conjunction with the PBE functional [39] to

compute the ZP and finite-temperature renormalization of the direct minimum gap of $MAPbI_3$, located at the BZ boundary point **R**. Figure 1 shows the temperature dependence of the band gap change obtained using different **q**-point grids to sample the vibrational BZ, and the inset shows the corresponding ZP corrections arising from quantum motion of the valence band maximum (VBM), conduction band minimum (CBM) and band gap. Appreciable convergence is reached on the temperature range 0-400 K with a $6 \times 6 \times 6$ **q**-point grid. However, as seen in the inset of Fig. 1, the very small ZP correction needs a denser **q**-point grid of $20 \times 20 \times 20$ to be accurately converged in the meV range.

Figure 1 shows that the electron-phonon coupling widens the band gap with increasing temperature, which is opposite to the behavior of most materials where temperature reduces the size of the band gap [55]. We find that thermal expansion further widens the band gap by 50 meV as temperature increases from 0 to 400 K, in agreement with earlier first-principles calculations [15, 56]. The band gap opening is in qualitative agreement with two recent experiments which also observe gap opening with increasing temperature [15, 16]. However, our calculated band gap change severely overestimates the one observed experimentally: calculations result in a band gap change of 120 meV between 290 K and 380 K, while the experimentally observed increase is only 30–40 meV [15, 16]. Figure S5 in the Supporting Information shows the temperature dependence of the band gaps at other points in the BZ, all indicate that the large change with temperature is not limited to the **R** zone boundary point, but rather is a general feature of the AHC theory in $MAPbI_3$.

To better understand the large discrepancy between experiment and theory, we examine temperature effects on the individual band edges at the **R** point. Ignoring thermal expansion, in the temperature range from 290 K to 380 K, the VBM decreases by 104 meV while the CBM increases by 43 meV. Experimentally, the VBM is observed to decrease by 110 meV, in agreement with our calculations, but at variance with our calculations, the CBM also shifts down by 77 meV [15].

The chemical character of the CBM is dominated by Pb atoms in $MAPbI_3$, and this suggests that the disagreement between theory and experiment might be due to the neglect of relativistic effects in our calculations so far. Indeed, SOC is needed to accurately calculate the static lattice band gap [25, 28]. To test the importance of SOC on our results, we have performed electron-phonon coupling calculations using the FD approach. Figure 2 compares the temperature dependence of the $MAPbI_3$ band gap without (FD-PBE-NSOC) and with (FD-PBE-SOC) spin-orbit coupling. In these calculations, we used the primitive cell (equivalent to sampling only the **Γ**-point of the vibrational BZ), and thus are not converged. Nevertheless, these results clearly demonstrate that SOC *enhances* the strength of electron-phonon coupling, almost doubling the band gap change with temperature. This shows that, although the proper description of electron-phonon coupling in $MAPbI_3$ requires SOC, its inclusion *worsens* the agreement between AHC theory and experiment.

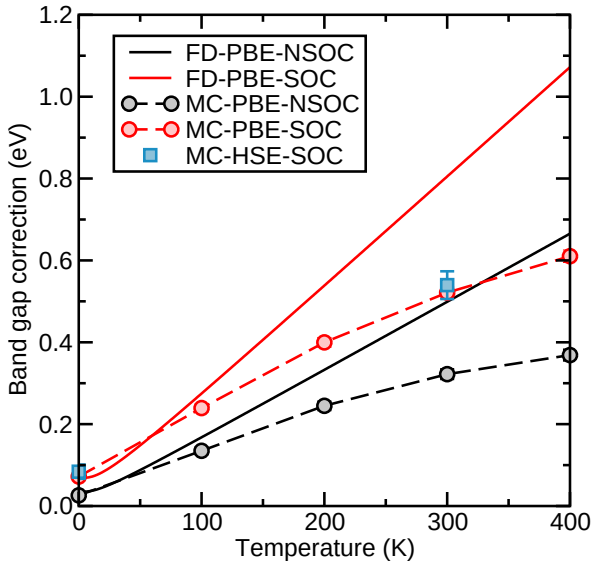

FIG. 2. Temperature dependence of the band gap of $MAPbI_3$ evaluated using the PBE functional and the FD approach without (NSOC) and with (SOC) spin-orbit coupling, and using the MC approach without and with SOC. Additional MC calculations are performed with the HSE functional and including SOC. The calculations are performed for the primitive cell, equivalent to sampling the **Γ**-point only. The statistical error bars in the MC results are included in all data points, but their size is smaller than the symbol size for some.

Another possible explanation for the discrepancy between the AHC theory and experiment is electron correlation, which can modify the strength of electron-phonon coupling in gapped systems [57, 58]. To test this, we have performed additional calculations using the hybrid HSE functional [40, 41]. Our results show that the inclusion of nonlocal correlation does not significantly affect the electron-phonon coupling strength. As a consequence, in the rest of the paper all calculations are performed using PBE+SOC.

Our analysis suggests that neither the inclusion of SOC nor a better description of exchange-correlation effects in the DFT functional, nor the rigid-ion approximation are responsible for the discrepancy between the AHC theory and experiment. The only possibility left is that the commonly used low-order expansion of electron-phonon coupling fails in $MAPbI_3$. Despite the successes of the AHC theory to describe the temperature dependence of the band structures of a wide range of materials [45, 48, 54, 59], recent calculations question the validity of the AHC theory in helium at terapascal pressures [60], molecular crystals at ambient conditions [61],

in the perovskite $CsSnI_3$ [62], and even (albeit moderately) in crystals like diamond [63].

To assess the importance of high-order terms in the evaluation of electron-phonon coupling in $MAPbI_3$, we compute Eq. (1) directly using a Monte Carlo (MC) method [47, 60]. We show the results in Fig. 2, obtained by sampling the vibrational BZ at the $\mathbf{\Gamma}$-point only. The ZP quantum corrections to the band gaps are similar between the FD and MC approaches, but their temperature dependence differs substantially. For example, for the curves including SOC, at 400 K, the FD change in the band gap overestimates the MC change by 460 meV. Thus, in $MAPbI_3$ high-order terms in the electron-phonon coupling are important, and the commonly used Eq. (2), with either DFPT or FD, fails in this system. Interestingly, to the authors knowledge, this is the first instance of the failure of the AHC theory that can be verified by direct comparison to experimental data.

The MC method is a real space method, and the convergence of the results with system size (equivalent to the convergence with respect to the BZ grid size) is particularly difficult. The computation of the electron-phonon coupling with cross-terms requires large diagonal supercells with sizes limited by the maximum number of atoms that can be realistically included in a DFT calculation. For $MAPbI_3$, the band gap correction in the temperature range 290–380 K is sufficiently converged with $3 \times 3 \times 3$ primitive cells, containing 324 atoms. Finite size effects are discussed in the Supporting Information based on the convergence of the AHC method in Fig. 1.

Figure 3 shows the temperature dependence of the $MAPbI_3$ band gap evaluated using the MC approach in conjunction with PBE + SOC in the temperature range from 290 to 380 K, relevant for solar cell applications. Thermal expansion effects on the results are also presented in the figure. For comparison, we show the results obtained from two experimental studies measured using optical absorbance or transmittance and photoluminescence spectroscopy [15, 16]. We only show the temperature range 290–380 K common to the two studies, and we do not distinguish between the tetragonal and cubic phases as argued before. The spread observed in the experimental data from the two measurement techniques is likely due to the presence of trap states below the band edges, but in both studies the band gap variations with temperature are less sensitive to experimental uncertainty and range between 30–40 meV. To avoid any complications arising from well-known errors of DFT in computing absolute band gaps, and to focus only on the band gap change with temperature, we shift the calculated temperature dependence such that at 329 K the value of the gap is 1.616 eV, given by the average of the experimental data.

The change in the experimental band gap of 30–40 meV in the temperature range of interest is in good agreement with the MC results that predict a change of 40 meV. Repeating the MC calculations using a $2 \times 2 \times 2$ supercell gives a change of 30 meV, also within the experimentally observed range. The change of the band gap originates from the VBM as the computed CBM correction is relatively flat in that temperature range, which is consistent with experiment [15]. By contrast, the AHC theory predicts a change of 120 meV in the band gap, severely overestimating the strength of electron-phonon coupling. These results are the first direct comparison of two leading first-principles methods to compute the temperature-dependence of band gaps where higher-order terms dominate, and for which an experimental measurement exists.

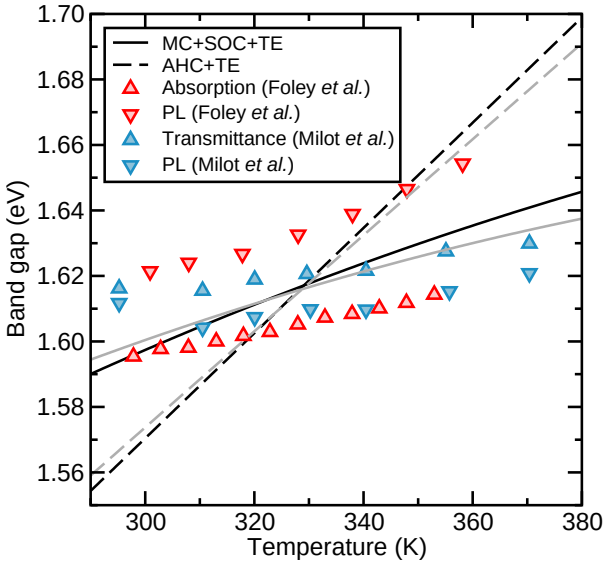

FIG. 3. Temperature dependence of the band gap of $MAPbI_3$ from Foley *et al.* [15] and from Milot *et al.* [16] using various techniques (red and blue triangles respectively), compared to the theoretical prediction using the MC approach (black solid line) and the AHC theory (dashed black line). Both theoretical lines include the effects of thermal expansion, but only the MC line includes SOC. The results neglecting thermal expansion are shown with gray lines.

Although the AHC theory fails to provide quantitatively accurate results for the strength of electron-phonon coupling in $MAPbI_3$, it is still useful in investigating the microscopic origin of the electron-phonon coupling strength, as each normal mode $(\mathbf{q}, \nu)$ appears independently in Eq. (2). Our results show that low-energy crystal modes dominate the coupling over the molecular high-energy modes. This is consistent with the fact that the VBM and CBM are formed by states whose character is dominated by Pb and I. It is interesting to note that the low-energy modes in $MAPbI_3$ also drive the tetragonal to cubic phase transition as temperature increases [56]. These results are also suggestive that the failure of the AHC theory is not due to high energy phonon modes as-

sociated with the organic molecule as these contribute the least to the energy renormalization. We have further investigated this point by calculating the temperature dependence of the band gap of the inorganic $CsPbI_3$ perovskite, where a similar picture emerges (see Supporting Information).

Overall, our results show that temperature drives the changes in the absolute value of the band gap of $MAPbI_3$, as well as in the shape of the band structure, from both electron-phonon coupling and thermal expansion. It has also been shown in previous work how the molecular orientation of the organic cation can modify these quantities [64, 65], and it would be interesting in future work to explore the combination of both effects.

Conclusions. We have determined the temperature dependence of the band gap and band edges of the cubic phase of $MAPbI_3$ using first-principles methods. Our results show that the $MAPbI_3$ band gap opens by 40 meV as temperature increases from 290 K to 380 K due to thermal expansion and electron-phonon coupling, which is in excellent agreement with the experimental value of 30-40 meV. Furthermore, we demonstrate that the calculation of electron-phonon coupling is particularly intricate, as we expose the limitations of the commonly used Allen-Heine-Cardona theory, arising from the dominant contribution in the electron-phonon coupling of high-order terms. We have also found that the use of the HSE hybrid functional has little effect, but the presence of Pb atoms means that the spin-orbit interaction substantially modifies the strength of electron-phonon coupling.

Overall, our Monte Carlo approach leads to good agreement between theory and experiment, and unambiguously confirms for the first time the importance of higher-order terms in the electron-phonon coupling. These results call for a revision of previous calculations of electron-phonon coupling in these materials, used for example to study their transport properties. We also hope that our findings will foster the design of new perovskite materials and the development of improved first-principles methods to efficiently tackle these challenging materials.

W.A.S. thanks Joshua J. Choi, Christian Carbogno, and Benjamin Folley for many useful discussions, and Laura Herz for sending the data used in Fig. 3. We also thank Mireia Crispin-Ortuzar for help in designing the graphical abstract. W.A.S. is supported in part by a start-up fund from the Department of Mechanical Engineering and Materials Science at the University of Pittsburgh. B.M. thanks Robinson College, Cambridge, and the Cambridge Philosophical Society for a Henslow Research Fellowship. Calculations were performed in part at the University of Pittsburgh Center for Simulation and Modeling. This work used the Extreme Science and Engineering Discovery Environment (XSEDE), which is supported by National Science Foundation grant number OCI-1053575.

* alsaidi@pitt.edu

[1] Akihiro Kojima, Kenjiro Teshima, Yasuo Shirai, and Tsutomu Miyasaka, "Organometal halide perovskites as visible-light sensitizers for photovoltaic cells," JACS **131**, 6050 (2009).

[2] Hui-Seon Kim, Chang-Ryul Lee, Jeong-Hyeok Im, Ki-Beom Lee, Thomas Moehl, Arianna Marchioro, Soo-Jin Moon, Robin Humphry-Baker, Jun-Ho Yum, Jacques E. Moser, Michael Grätzel, and Nam-Gyu Park, "Lead iodide perovskite sensitized all-solid-state submicron thin film mesoscopic solar cell with efficiency exceeding 9%," Sci. Rep. **2** (2012).

[3] Michael M. Lee, Jol Teuscher, Tsutomu Miyasaka, Takurou N. Murakami, and Henry J. Snaith, "Efficient hybrid solar cells based on meso-superstructured organometal halide perovskites," Science **338**, 643 (2012).

[4] Julian Burschka, Norman Pellet, Soo-Jin Moon, Robin Humphry-Baker, Peng Gao, Mohammad K. Nazeeruddin, and Michael Grätzel, "Sequential deposition as a route to high-performance perovskite-sensitized solar cells," Nature **499**, 316 (2013).

[5] Henry J. Snaith, "Perovskites: The emergence of a new era for low-cost, high-efficiency solar cells," J. Phys. Chem. Lett. **4**, 3623 (2013).

[6] Guichuan Xing, Nripan Mathews, Shuangyong Sun, Swee Sien Lim, Yeng Ming Lam, Michael Grätzel, Subodh Mhaisalkar, and Tze Chien Sum, "Long-range balanced electron- and hole-transport lengths in organic-inorganic $CH_3NH_3PbI_3$," Science **342**, 344 (2013).

[7] Gary Hodes, "Perovskite-based solar cells," Science **342**, 317 (2013).

[8] NREL Best Research-Cell Efficiencies Chart.

[9] R. A. Marcus, "On the theory of electron-transfer reactions. VI. Unified treatment for homogeneous and electrode reactions," J. Chem. Phys. **43**, 679 (1965).

[10] Philip Schulz, Eran Edri, Saar Kirmayer, Gary Hodes, David Cahen, and Antoine Kahn, "Interface energetics in organo-metal halide perovskite-based photovoltaic cells," Energy Environ. Sci. **7**, 1377 (2014).

[11] S. M. Sze and K. K. NG, *Physics of Semiconductor devices* (Wiley, New Jersey, 2007).

[12] K. Emery, J. Burdick, Y. Caiyem, D. Dunlavy, H. Field, B. Kroposki, T. Moriarty, L. Ottoson, S. Rummel, T. Strand, and M. W. Wanlass, "Temperature dependence of photovoltaic cells, modules and systems," in *Photovoltaic Specialists Conference, 1996., Conference Record of the Twenty Fifth IEEE* (1996) pp. 1275–1278.

[13] E. Skoplaki, A.G. Boudouvis, and J.A. Palyvos, "A simple correlation for the operating temperature of photovoltaic modules of arbitrary mounting," Sol. Energy Mater. Sol. Cells **92**, 1393 (2008).

[14] Hua Zhang, Xianfeng Qiao, Yan Shen, Thomas Moehl, Shaik M. Zakeeruddin, Michael Grätzel, and Mingkui Wang, "Photovoltaic behaviour of lead methylammonium triiodide perovskite solar cells down to 80 K," J. Mater. Chem. A **3**, 11762 (2015).

[15] Benjamin J. Foley, Daniel L. Marlowe, Keye Sun, Wissam A. Saidi, Louis Scudiero, Mool C. Gupta, and Joshua J. Choi, "Temperature dependent energy levels of methylammonium lead iodide perovskite," Appl. Phys.

Lett. **106**, 243904 (2015).
[16] Rebecca L. Milot, Giles E. Eperon, Henry J. Snaith, Michael B. Johnston, and Laura M. Herz, "Temperature-dependent charge-carrier dynamics in $CH_3NH_3PbI_3$ perovskite thin films," Adv. Funct. Mater. **25**, 6218 (2015).
[17] Sneha A. Kulkarni, Tom Baikie, Pablo P. Boix, Natalia Yantara, Nripan Mathews, and Subodh Mhaisalkar, "Band-gap tuning of lead halide perovskites using a sequential deposition process," J. Mater. Chem. A **2**, 9221 (2014).
[18] Edoardo Mosconi, Anna Amat, Md. K. Nazeeruddin, Michael Grätzel, and Filippo De Angelis, "First-principles modeling of mixed halide organometal perovskites for photovoltaic applications," J. Phys. Chem. C **117**, 13902 (2013).
[19] Marina R. Filip, Giles E. Eperon, Henry J. Snaith, and Feliciano Giustino, "Steric engineering of metal-halide perovskites with tunable optical band gaps," Nat. Commun. **5**, 5757 (2014).
[20] George Volonakis, Marina R. Filip, Amir Abbas Haghighirad, Nobuya Sakai, Bernard Wenger, Henry J. Snaith, and Feliciano Giustino, "Lead-free halide double perovskites via heterovalent substitution of noble metals," J. Phys. Chem. Lett. **7**, 1254 (2016).
[21] Rebecka Lindblad, Dongqin Bi, Byung wook Park, Johan Oscarsson, Mihaela Gorgoi, Hans Siegbahn, Michael Odelius, Erik M. J. Johansson, and Håkan Rensmo, "Electronic structure of $TiO_2/CH_3NH_3PbI_3$ perovskite solar cell interfaces," J. Phys. Chem. Lett. **5**, 648 (2014).
[22] Edoardo Mosconi, Enrico Ronca, and Filippo De Angelis, "First-principles investigation of the TiO_2/organohalide perovskites interface: The role of interfacial chlorine," J. Phys. Chem. Lett. **5**, 2619 (2014).
[23] Tom Baikie, Yanan Fang, Jeannette M. Kadro, Martin Schreyer, Fengxia Wei, Subodh G. Mhaisalkar, Michael Grätzel, and Tim J. White, "Synthesis and crystal chemistry of the hybrid perovskite $(CH_3NH_3)PbI_3$ for solid-state sensitised solar cell applications," J. Mater. Chem. A **1**, 5628 (2013).
[24] Federico Brivio, Alison B. Walker, and Aron Walsh, "Structural and electronic properties of hybrid perovskites for high-efficiency thin-film photovoltaics from first-principles," APL Mater. **1**, 042111 (2013).
[25] Jacky Even, Laurent Pedesseau, Jean-Marc Jancu, and Claudine Katan, "Importance of spin-orbit coupling in hybrid organic/inorganic perovskites for photovoltaic applications," J. Phys. Chem. Lett. **4**, 2999 (2013).
[26] Paolo Umari, Edoardo Mosconi, and Filippo De Angelis, "Relativistic *GW* calculations on $CH_3NH_3PbI_3$ and $CH_3NH_3SnI_3$ perovskites for solar cell applications," Sci. Rep. **4**, 4467 (2014).
[27] Federico Brivio, Keith T. Butler, Aron Walsh, and Mark van Schilfgaarde, "Relativistic quasiparticle self-consistent electronic structure of hybrid halide perovskite photovoltaic absorbers," Phys. Rev. B **89**, 155204 (2014).
[28] Marina R. Filip and Feliciano Giustino, "*GW* quasiparticle band gap of the hybrid organic-inorganic perovskite $CH_3NH_3PbI_3$: Effect of spin-orbit interaction, semicore electrons, and self-consistency," Phys. Rev. B **90**, 245145 (2014).
[29] P. B. Allen and V. Heine, "Theory of the temperature dependence of electronic band structures," J. Phys. C **9**, 2305 (1976).
[30] P. B. Allen and M. Cardona, "Theory of the temperature dependence of the direct gap of germanium," Phys. Rev. B **23**, 1495 (1981).
[31] P. Hohenberg and W. Kohn, "Inhomogeneous electron gas," Phys. Rev. **136**, B864–B871 (1964).
[32] W. Kohn and L. J. Sham, "Self-consistent equations including exchange and correlation effects," Phys. Rev. **140**, A1133–A1138 (1965).
[33] M. C. Payne, M. P. Teter, D. C. Allan, T. A. Arias, and J. D. Joannopoulos, "Iterative minimization techniques for *ab initio* total-energy calculations: molecular dynamics and conjugate gradients," Rev. Mod. Phys. **64**, 1045–1097 (1992).
[34] G. Kresse and J. Hafner, "*Ab initio* molecular dynamics for liquid metals," Phys. Rev. B **47**, 558 (1993).
[35] G. Kresse and J. Hafner, "*Ab initio* molecular-dynamics simulation of the liquid-metal-amorphous-semiconductor transition in germanium," Phys. Rev. B **49**, 14251 (1994).
[36] G. Kresse and J. Furthmüller, "Efficiency of *ab-initio* total energy calculations for metals and semiconductors using a plane-wave basis set," Comput. Mater. Sci. **6**, 15 (1996).
[37] G. Kresse and J. Furthmüller, "Efficient iterative schemes for *ab initio* total-energy calculations using a plane-wave basis set," Phys. Rev. B **54**, 11169 (1996).
[38] X. Gonze, F. Jollet, F. Abreu Araujo, D. Adams, B. Amadon, T. Applencourt, C. Audouze, J.-M. Beuken, J. Bieder, A. Bokhanchuk, E. Bousquet, F. Bruneval, D. Caliste, M. Côté, F. Dahm, F. Da Pieve, M. Delaveau, M. Di Gennaro, B. Dorado, C. Espejo, G. Geneste, L. Genovese, A. Gerossier, M. Giantomassi, Y. Gillet, D.R. Hamann, L. He, G. Jomard, J. Laflamme Janssen, S. Le Roux, A. Levitt, A. Lherbier, F. Liu, I. Lukačević, A. Martin, C. Martins, M.J.T. Oliveira, S. Poncé, Y. Pouillon, T. Rangel, G.-M. Rignanese, A.H. Romero, B. Rousseau, O. Rubel, A.A. Shukri, M. Stankovski, M. Torrent, M.J. Van Setten, B. Van Troeye, M.J. Verstraete, D. Waroquiers, J. Wiktor, B. Xu, A. Zhou, and J.W. Zwanziger, "Recent developments in the ABINIT software package," Comput. Phys. Comm. **205**, 106 (2016).
[39] John P. Perdew, Kieron Burke, and Matthias Ernzerhof, "Generalized gradient approximation made simple," Phys. Rev. Lett. **77**, 3865 (1996).
[40] J. Paier, M. Marsman, K. Hummer, G. Kresse, I. C. Gerber, and J. G. Ángyán, "Screened hybrid density functionals applied to solids," J. Chem. Phys. **124**, 154709 (2006).
[41] J. Paier, M. Marsman, K. Hummer, G. Kresse, I. C. Gerber, and J. G. Ángyán, "Erratum: Screened hybrid density functionals applied to solids [J. Chem. Phys. 124, 154709 (2006)]," J. Chem. Phys. **125**, 249901 (2006).
[42] A. Poglitsch and D. Weber, "Dynamic disorder in methylammoniumtrihalogenoplumbates (II) observed by millimeterwave spectroscopy," J. Chem. Phys. **87**, 6373 (1987).
[43] Constantinos C. Stoumpos, Christos D. Malliakas, and Mercouri G. Kanatzidis, "Semiconducting tin and lead iodide perovskites with organic cations: Phase transitions, high mobilities, and near-infrared photoluminescent properties," Inorg. Chem. **52**, 9019 (2013).
[44] Lucy D. Whalley, Jonathan M. Skelton, Jarvist M. Frost, and Aron Walsh, "Phonon anharmonicity, lifetimes and

thermal transport in $CH_3NH_3PbI_3$ from many-body perturbation theory," arXiv:1609.00825 (2016).
[45] Feliciano Giustino, Steven G. Louie, and Marvin L. Cohen, "Electron-phonon renormalization of the direct band gap of diamond," Phys. Rev. Lett. **105**, 265501 (2010).
[46] Elena Cannuccia and Andrea Marini, "Effect of the quantum zero-point atomic motion on the optical and electronic properties of diamond and trans-polyacetylene," Phys. Rev. Lett. **107**, 255501 (2011).
[47] Christopher E. Patrick and Feliciano Giustino, "Quantum nuclear dynamics in the photophysics of diamondoids," Nat. Commun. **4**, 2006 (2013).
[48] Bartomeu Monserrat and R. J. Needs, "Comparing electron-phonon coupling strength in diamond, silicon, and silicon carbide: First-principles study," Phys. Rev. B **89**, 214304 (2014).
[49] S. Poncé, G. Antonius, P. Boulanger, E. Cannuccia, A. Marini, M. Côté, and X. Gonze, "Verification of first-principles codes: Comparison of total energies, phonon frequencies, electron-phonon coupling and zero-point motion correction to the gap between ABINIT and QE/Yambo," Comput. Mater. Sci. **83**, 341 (2014).
[50] Feliciano Giustino, "Electron-phonon interactions from first principles," arXiv:1603.06965 (2016).
[51] K. Kunc and Richard M. Martin, "*Ab Initio* force constants of GaAs: A new approach to calculation of phonons and dielectric properties," Phys. Rev. Lett. **48**, 406 (1982).
[52] Jonathan H. Lloyd-Williams and Bartomeu Monserrat, "Lattice dynamics and electron-phonon coupling calculations using nondiagonal supercells," Phys. Rev. B **92**, 184301 (2015).
[53] A description of the use of the rigid-ion approximation in the context of the AHC theory can be found in Ref. 66.
[54] S. Poncé, Y. Gillet, J. Laflamme Janssen, A. Marini, M. Verstraete, and X. Gonze, "Temperature dependence of the electronic structure of semiconductors and insulators," J. Chem. Phys. **143**, 102813 (2015).
[55] Manuel Cardona and M. L. W. Thewalt, "Isotope effects on the optical spectra of semiconductors," Rev. Mod. Phys. **77**, 1173–1224 (2005).
[56] Wissam A. Saidi and Joshua J. Choi, "Nature of the cubic to tetragonal phase transition in methylammonium lead iodide perovskite," J. Chem. Phys. **145**, 144702 (2016).
[57] G. Antonius, S. Poncé, P. Boulanger, M. Côté, and X. Gonze, "Many-body effects on the zero-point renormalization of the band structure," Phys. Rev. Lett. **112**, 215501 (2014).
[58] Bartomeu Monserrat, "Correlation effects on electron-phonon coupling in semiconductors: Many-body theory along thermal lines," Phys. Rev. B **93**, 100301 (2016).
[59] Peng Han and Gabriel Bester, "Large nuclear zero-point motion effect in semiconductor nanoclusters," Phys. Rev. B **88**, 165311 (2013).
[60] Bartomeu Monserrat, N. D. Drummond, Chris J. Pickard, and R. J. Needs, "Electron-phonon coupling and the metallization of solid helium at terapascal pressures," Phys. Rev. Lett. **112**, 055504 (2014).
[61] Bartomeu Monserrat, Edgar A. Engel, and Richard J. Needs, "Giant electron-phonon interactions in molecular crystals and the importance of nonquadratic coupling," Phys. Rev. B **92**, 140302 (2015).
[62] Christopher E. Patrick, Karsten W. Jacobsen, and Kristian S. Thygesen, "Anharmonic stabilization and band gap renormalization in the perovskite $CsSnI_3$," Phys. Rev. B **92**, 201205 (2015).
[63] G. Antonius, S. Poncé, E. Lantagne-Hurtubise, G. Auclair, X. Gonze, and M. Côté, "Dynamical and anharmonic effects on the electron-phonon coupling and the zero-point renormalization of the electronic structure," Phys. Rev. B **92**, 085137 (2015).
[64] Edoardo Mosconi, Claudio Quarti, Tanja Ivanovska, Giampiero Ruani, and Filippo De Angelis, "Structural and electronic properties of organo-halide lead perovskites: a combined IR-spectroscopy and *ab initio* molecular dynamics investigation," Phys. Chem. Chem. Phys. **16**, 16137 (2014).
[65] Carlo Motta, Fedwa El-Mellouhi, Sabre Kais, Nouar Tabet, Fahhad Alharbi, and Stefano Sanvito, "Revealing the role of organic cations in hybrid halide perovskite $CH_3NH_3PbI_3$," Nat. Commun. **6**, 7026 (2015).
[66] S. Poncé, G. Antonius, Y. Gillet, P. Boulanger, J. Laflamme Janssen, A. Marini, M. Côté, and X. Gonze, "Temperature dependence of electronic eigenenergies in the adiabatic harmonic approximation," Phys. Rev. B **90**, 214304 (2014).
[67] P. E. Blöchl, "Projector augmented-wave method," Phys. Rev. B **50**, 17953 (1994).
[68] G. Kresse and D. Joubert, "From ultrasoft pseudopotentials to the projector augmented-wave method," Phys. Rev. B **59**, 1758 (1999).
[69] Xavier Gonze and Changyol Lee, "Dynamical matrices, born effective charges, dielectric permittivity tensors, and interatomic force constants from density-functional perturbation theory," Phys. Rev. B **55**, 10355 (1997).
[70] X. Gonze, P. Boulanger, and M. Côté, "Theoretical approaches to the temperature and zero-point motion effects on the electronic band structure," Ann. Phys. **523**, 168–178 (2011).
[71] R. W. Godby, M. Schlüter, and L. J. Sham, "Accurate exchange-correlation potential for silicon and its discontinuity on addition of an electron," Phys. Rev. Lett. **56**, 2415–2418 (1986).
[72] R. W. Godby, M. Schlüter, and L. J. Sham, "Self-energy operators and exchange-correlation potentials in semiconductors," Phys. Rev. B **37**, 10159–10175 (1988).
[73] Alexandre Tkatchenko and Matthias Scheffler, "Accurate molecular van der Waals interactions from ground-state electron density and free-atom reference data," Phys. Rev. Lett. **102**, 073005 (2009).

Supporting Information for "Temperature Dependence of the Energy Levels of Methylammonium Lead Iodide Perovskite from First Principles"

COMPUTATIONAL DETAILS

Most calculations reported in the main text have been performed using the plane-wave DFT code VASP [S34–S37]. We use the PBE [S39] and HSE [S40, S41] functionals as described in the text, together with the projector augmented-wave method [S67, S68]. The energy cut-off used is 500 eV, and the electronic Brillouin zone (BZ) is sampled using a $6\times6\times6$ grid for the primitive cell, and commensurate grids for the supercells. Spin-orbit coupling (SOC) is included as described in the text.

The vibrational harmonic calculations have been done using the finite displacement method in conjunction with nondiagonal supercells [S52]. The electron-phonon coupling calculations using the FD approach have also been performed using the finite displacement approach and nondiagonal supercells. The non-adiabatic Allen-Heine-Cardona calculations based on DFPT have been performed with the ABINIT software [S38] using a $6\times6\times6$ $\mathbf{\Gamma}$-centered $\mathbf{k}$-point grid with a plane-wave energy cutoff of 680 eV. Norm-conserving pseudopotential with the PBE functional have been used. The vibrational BZ was sampled using grids of sizes up to $20\times20\times20$.

The cubic cell that we have used in our calculations exhibits some imaginary phonon frequencies, reflecting the dynamical instability of this structure, and driving it towards the lower-temperature tetragonal and orthorhombic structures. In the calculations reported in the main manuscript, we have set the amplitudes of the vibrational modes corresponding to imaginary frequencies to zero, to be able to work with the cubic structure. We have performed additional calculations for the $2\times2\times2$ supercell in which we have allowed the imaginary modes to contribute to electron-phonon coupling by describing them using Gaussian vibrational wave functions of amplitude given by the absolute value of their (imaginary) frequencies, in the spirit of the self-consistent harmonic approximation. Our calculations show that the temperature dependence does not change within error bars whether the unstable modes are allowed to contribute or not.

EXPANSION ORDER IN THE ELECTRON-PHONON INTERACTION

The electronic state average over atomic vibrations

$$\epsilon_{\mathbf{k}n}(T)=\frac{1}{\mathcal{Z}}\sum_{\mathbf{s}}\langle\chi_{\mathbf{s}}|\epsilon_{\mathbf{k}n}|\chi_{\mathbf{s}}\rangle e^{-E_{\mathbf{s}}/k_{\mathrm{B}}T}, \tag{S1}$$

is usually performed using a *quadratic approximation* to the dependence of $\epsilon_{\mathbf{k}n}$ on the atomic configuration. In terms of normal modes of vibration $u_{\mathbf{q}\nu}$ characterized by a wave vector $\mathbf{q}$ with branch ν, the value of the electronic state at a general atomic configuration $\mathbf{u}=\{u_{\mathbf{q}\nu}\}$ can be expanded around its equilibrium position as

$$\epsilon_{\mathbf{k}n}(\mathbf{u})=\epsilon_{\mathbf{k}n}(\mathbf{0})+\sum_{\mathbf{q},\nu}a^{(1)}_{\mathbf{q}\nu}u_{\mathbf{q}\nu}+\sum_{\mathbf{q},\nu,\mathbf{q}',\nu'}a^{(2)}_{\mathbf{q}\nu;\mathbf{q}'\nu'}u^{*}_{\mathbf{q}\nu}u_{\mathbf{q}'\nu'}+\cdots, \tag{S2}$$

where $\{a^{(1)}_{\mathbf{q}\nu},a^{(2)}_{\mathbf{q}\nu;\mathbf{q}'\nu'},\ldots\}$ are the electron-phonon coupling constants. Truncating this expansion at second order and substituting into Eq. (S1) leads to

$$\Delta\epsilon_{\mathbf{k}n}(T)\triangleq\epsilon_{\mathbf{k}n}(T)-\epsilon_{\mathbf{k}n}(\mathbf{0})=\frac{1}{N_{\mathbf{q}}}\sum_{\mathbf{q},\nu}\frac{a^{(2)}_{\mathbf{q}\nu;\mathbf{q}\nu}}{\omega_{\mathbf{q}\nu}}\left[\frac{1}{2}+n_{\mathrm{B}}(\omega_{\mathbf{q}\nu},T)\right], \tag{S3}$$

where $\Delta\epsilon_{\mathbf{k}n}(T)$ is the phonon renormalization of the electronic state at temperature T, $N_{\mathbf{q}}$ is the number of points in the vibrational BZ, $\omega_{\mathbf{q}\nu}$ is the harmonic frequencies of mode $(\mathbf{q},\nu)$, and n_{B} is a Bose-Einstein factor. The expression in Eq. (S3) is computationally convenient, as the coupling constants of interest only depend on individual modes, and can be efficiently calculated using density functional perturbation theory (DFPT) [S69] or finite displacements [S51].

To obtain a DFPT formulation of Eq. (S3), the second-order coupling constants are expressed as [S66]

$$a^{(2)}_{\mathbf{q}\nu;\mathbf{q}\nu}=\frac{1}{2}\Big[\mathbf{F}_{\mathbf{q}\nu}u^{*}_{\mathbf{q}\nu}u_{\mathbf{q}\nu}+\mathbf{D}_{\mathbf{q}\nu}u^{*}_{\mathbf{q}\nu}u_{\mathbf{q}\nu}\Big], \tag{S4}$$

where $\mathbf{F}_{\mathbf{q}\nu} = \frac{1}{2}[\langle\psi^{(1)}_{\mathbf{k},\mathbf{q},n}|\hat{H}^{(1)}_{\mathbf{k}+\mathbf{q},\mathbf{k}}|\psi^{(0)}_{\mathbf{k}n}\rangle + (c.c.)]$ is the Fan term of the periodic part of the electronic wavefunction $|\psi^{(0)}\rangle$ with Hamiltonian $\hat{H}$, $\hat{H}^{(1)}$ is the first-order change of the Hamiltonian due to a lattice distortion arising from nuclear vibrations, and $|\psi^{(1)}\rangle$ is the corresponding first-order change in the wavefunction. $\mathbf{D}_{\mathbf{q}\nu} = \langle\psi^{(0)}_{\mathbf{k}n}|\hat{H}^{(2)}_{\mathbf{k}-\mathbf{q},\mathbf{k}+\mathbf{q}}|\psi^{(0)}_{\mathbf{k}n}\rangle$ is the Debye-Waller (DW) term arising from the second-order change of the Hamiltonian due to nuclear vibrations. Using the rigid-ion approximation to recast the DW term in terms of first-order matrix elements that are directly accessible through routine DFPT calculations, one obtains the so-called Allen-Heine-Cardona theory [S29, S30]. Part of the DW term is neglected in the process, hence the approximation. The part of the DW term neglected by the rigid-ion approximation has been found to be small in crystals [S66] but crucial for molecules [S70]. Thanks to this approximation, very fine BZ grids can be used to fully converge the results [S54]. In the main manuscript, this approximation is referred to as *Allen-Heine-Cardona theory* (AHC).

To obtain the finite displacement formulation of Eq. (S3), the second-order coupling constants are expressed as

$$a^{(2)}_{\mathbf{q}\nu;\mathbf{q}\nu} = \frac{\epsilon_{\mathbf{k}n}(u_{\mathbf{q}\nu}) + \epsilon_{\mathbf{k}n}(-u_{\mathbf{q}\nu})}{2u^2_{\mathbf{q}\nu}}, \tag{S5}$$

and explicit atomic displacements $\pm u_{\mathbf{q}\nu}$ are used to evalute the changes in the electronic eigenenergies. The finite displacement formulation does not rely on the rigid-ion approximation, but the vibrational BZ can only be sampled by explicitly constructing supercells of the primitive cell. Until recently, the fine BZ grids needed to converge the evaluation of electron-phonon coupling in this context made the calculations using the finite displacement method prohibitive, due to the large supercell sizes required. This situation has improved significantly thanks to the introduction of nondiagonal supercells, that provide access to very fine BZ grids using moderate supercells sizes, and approaching the levels of convergence available using DFPT [S52]. In the main manuscript, this approximation is referred to as *finite displacements* (FD).

Despite the successes of the quadratic theory (AHC or FD) to describe the temperature dependence of the band structures of a range of materials, recent calculations question the validity of the AHC theory in helium at terapascal pressures [S60], molecular crystals at ambient conditions [S61], in the perovskite $CsSnI_3$ [S62], and even (albeit moderately) in crystals like diamond [S63] because higher-order terms in the expansion of Eq. (S2) make significant contributions. These terms can be included by evaluating Eq. (S1) directly using Monte Carlo integration

$$\epsilon_{\mathbf{k}n}(T) \simeq \frac{1}{M}\sum_{i=1}^{M}\epsilon_{\mathbf{k}n}(\mathbf{u}_i), \tag{S6}$$

where M is the number of sampling points, distributed according to the vibrational density. The use of Monte Carlo integration leads to statistical error bars in the Monte Carlo estimates of the integrals, which are given by

$$\delta\epsilon_{\mathbf{k}n}(T) \simeq \left[\frac{1}{M(M-1)}\sum_{i=1}^{M}\left(\epsilon_{\mathbf{k}n}(\mathbf{u}_i) - \frac{1}{M}\sum_{j=1}^{M}\epsilon_{\mathbf{k}n}(\mathbf{u}_j)\right)^2\right]^{1/2}. \tag{S7}$$

Error bars are included in all results obtained using Monte Carlo integration, and if they cannot be seen in a given plot, that means that their size is smaller than the size of the point shown.

We emphasize here that the vibrational wave function is treated within the harmonic approximation, even when the higher order terms are included in the description of the coupling of vibrations to electronic eigenstates. Within the harmonic approximation, the vibrational density at temperature T is given by a product of Gaussian functions over the normal modes $\prod_{\mathbf{q},\nu}(2\pi\sigma^2_{\mathbf{q}\nu})^{-1/2}\exp(-\frac{u^2_{\mathbf{q}\nu}}{2\sigma^2_{\mathbf{q}\nu}})$ of amplitude

$$\sigma^2_{\mathbf{q}\nu}(T) = \frac{1}{\omega_{\mathbf{q}\nu}}\coth\left(\frac{\omega_{\mathbf{q}\nu}}{k_{\mathrm{B}}T}\right), \tag{S8}$$

where k_{B} is Boltzmann's constant. While this approach fully accounts for all higher-order terms in electron-phonon coupling, the presence of cross-terms between different modes means that it cannot be used with DFPT or nondiagonal supercells, and therefore the computational advantages that these methods provide cannot be exploited. In the main manuscript, this approach is refereed to as the *Monte Carlo approach* (MC).

In Fig. S1 we compare the temperature dependence of the band gap of $MAPbI_3$ using the three different methods described above. The two approaches based on the quadratic expansion of Eq. (S2), AHC and FD, show a significant

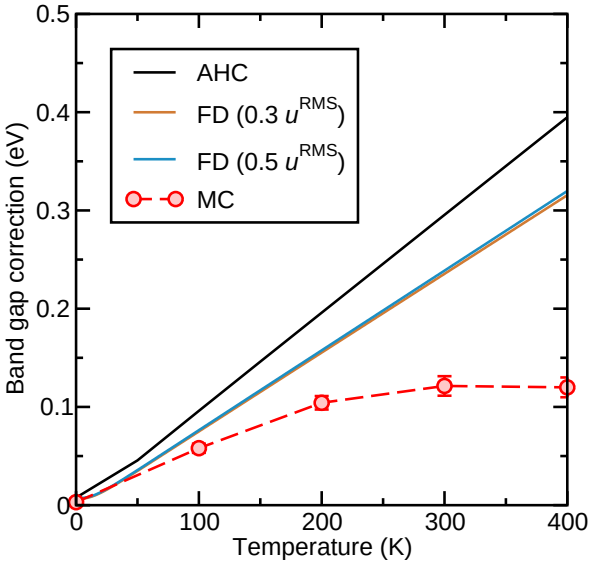

FIG. S1. Temperature dependence of the band gap of $MAPbI_3$ evaluated using the AHC theory within DFPT (black lines), the quadratic approximation within a FD approach (blue and orange lines), and the MC sampling approach (red circles). For the FD approach, two sets of calculations have been performed, with finite displacement amplitudes given by $0.3u^{\rm RMS}$ and $0.5u^{\rm RMS}$ where $u^{\rm RMS} = \sqrt{\langle u^2 \rangle}$. The calculations have been performed by sampling a $2 \times 2 \times 2$ vibrational Brillouin zone grid, and without spin-orbit coupling. The statistical error bars in the MC results are included, but for the low temperature data points their size is smaller than the symbol size.

increase in the value of the band gap with temperature, reaching 0.3-0.4 eV at 400 K. The disagreement between the two quadratic methods approaches 70 meV at 400 K. The origin of this discrepancy could be attributed to various factors. First, the AHC calculations have been performed with the ABINIT package [S38], while the FD calculations have been performed with the VASP package [S34–S37]. Different pseudopotentials and slightly different atomic coordinates have been used (although the volumes were the same).

In Fig. S1 we compare the temperature dependence of the band gap of $MAPbI_3$ using the three different methods described above. The two approaches based on the quadratic expansion of Eq. (S2), AHC and FD, show a significant increase in the value of the band gap with temperature, reaching 0.3-0.4 eV at 400 K. The disagreement between the two quadratic methods approaches 70 meV at 400 K. The origin of this discrepancy could be attributed to various factors. First, the AHC calculations have been performed with the ABINIT package [S38], while the FD calculations have been performed with the VASP package [S34–S37]. Different pseudopotentials and slightly different atomic coordinates have been used (although the volumes were the same). Given the above-mentioned differences, the agreement between the two methods is quite satisfactory. This leads us to believe that the rigid-ion approximation involved in the AHC approach seems to hold for molecular crystals. A more throughout investigation would be required to confirm this.

In any case, Fig. S1 clearly shows that the quadratic methods are not appropriate for the description of electron-phonon coupling in $MAPbI_3$, as they significantly overestimate the strength of the electron-phonon coupling. The higher-order terms included in the MC approach lead to a different temperature dependence of the band gap, and as shown in the main manuscript, agreement with experiment is only obtained if these higher-order terms are included.

ELECTRONIC STRUCTURE METHOD

In the main manuscript, we have established that the inclusion of SOC is necessary for an accurate description of the strength of the electron-phonon coupling in $MAPbI_3$, but that nonlocal electronic correlations are not important. Here, we provide further details of those calculations.

In evaluating Eq. (S1), both electronic states and phonons are usually treated within semilocal DFT. However, semilocal DFT is known to severely underestimate band gaps in semiconductors and insulators [S71, S72]. In $MAPbI_3$, the situation is somewhat complex. The experimental band gap is 1.6 eV [S23], and semilocal DFT predicts a band gap of about 1.6 eV [S24], which appears to be in good agreement with experiment. Nevertheless, the presence of Pb atoms means that SOC is strong in $MAPbI_3$, and its inclusion in the calculations reduces the band gap by around

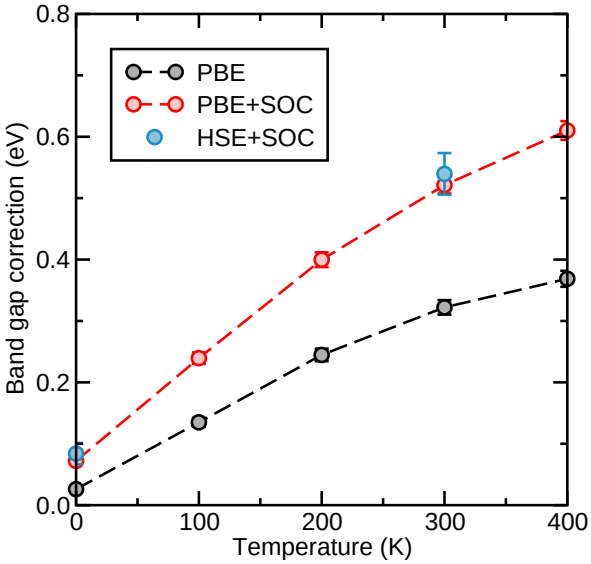

FIG. S2. Temperature dependence of the band gap of $MAPbI_3$ evaluated using PBE (black circles), PBE+SOC (red circles), and HSE+SOC (blue circles), and the MC method. Only the electron-phonon coupling constants for $\mathbf{\Gamma}$-point phonons are included. The statistical error bars are included in all data points, although they are not visible in some as their size is smaller than the symbol size.

1.0 eV [S25], so that indeed semilocal DFT underestimates the band gap. Performing calculations using hybrid functionals including SOC brings the gap closer to the experimental value, and GW+SOC calculations lead to band gaps in very good agreement with experiment [S26–S28]. It had been assumed for some time that, while electronic states were poorly reproduced by semilocal DFT, electron-phonon coupling was well-described by this level of theory, as only *changes* in band gaps need to be calculated. However, it has recently been shown that in some materials semilocal DFT severely underestimates the strength of electron-phonon coupling [S57, S58].

Using MC sampling, we evaluate the temperature dependence of the band gap of $MAPbI_3$ using PBE, PBE+SOC, and HSE+SOC, by focusing again on the $\mathbf{\Gamma}$-point phonons. The results are shown in Fig. S2. The inclusion of SOC significantly increases the strength of the electron-phonon coupling, such that at 500 K, the band gap change is underestimated by 0.28 eV if the SOC is neglected. The effects of SOC arise exclusively from the CBM, which is mostly of Pb character. For example, at 300 K, the change in the VBM is -0.24 eV both without and with SOC, but the change in the CBM is $+0.08$ eV without SOC, and increases to $+0.28$ eV with SOC.

The use of the hybrid functional HSE [S40, S41] instead of PBE does not seem to make a significant difference. As a consequence, the final results in the main manuscript are obtained using PBE+SOC.

BRILLOUIN ZONE SAMPLING

Using the quadratic theory of Eq. (S3), it has been shown that the strength of electron-phonon coupling converges slowly as a function of vibrational BZ grid size [S52, S54]. Unfortunately, the quadratic theory is not applicable to $MAPbI_3$ due to the importance of high-order terms, and that the methods developed to accurately sample the BZ cannot be used here. For the MC sampling method, supercells of the primitive cell need to be constructed, and their sizes are limited by the maximum number of atoms that can be realistically included in a DFT calculation. In our case, we find that we can reach system sizes of $3 \times 3 \times 3$ primitive cells, containing 324 atoms.

In Fig. S3 we show the temperature dependence of the band gap of $MAPbI_3$ for supercells of varying sizes, and it is clear that the band gap change is not converged for the largest supercells studied. Nonetheless, the changes arising from using supercells of varying size are smaller than either the changes induced by including higher-order terms or the SOC interaction. Furthermore, the change in the band gap at the relevant temperatures for solar cell applications, of above 300 K, is similar between the $2 \times 2 \times 2$ and the $3 \times 3 \times 3$ supercells, and the difference is smaller than the experimental uncertainty in the available data. Therefore, our final results in the main manuscript are reported for the $3 \times 3 \times 3$ supercell.

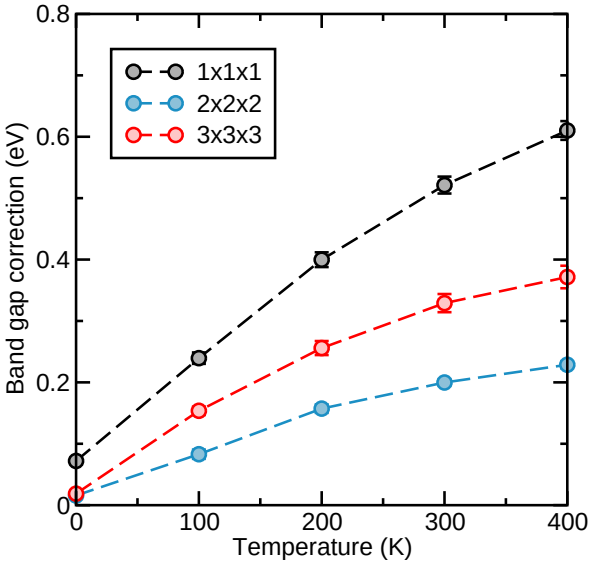

FIG. S3. Temperature dependence of the band gap of $MAPbI_3$ evaluated using supercells of sizes $1 \times 1 \times 1$ (black circles), $2 \times 2 \times 2$ (blue circles), and $3 \times 3 \times 3$ (red circles). The statistical error bars are included in all data points, although they are not visible in some as their size is smaller than the symbol size.

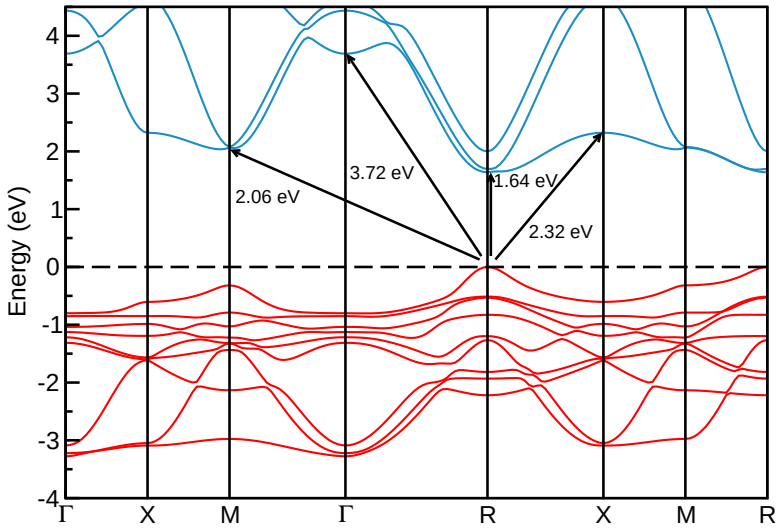

FIG. S4. Static lattice band structure of $MAPbI_3$ calculated using the PBE functional without including SOC. The dashed line indicates the position of the Fermi level.

RESULTS USING THE AHC THEORY AND MC SAMPLING

In this section we describe several results obtained using the AHC theory and MC sampling. In Fig. S4 we show the static lattice band structure of $MAPbI_3$ calculated using the PBE functional without the inclusion of SOC. The values of several band gaps from the valence band maximum (VBM) at the $\mathbf{R} = (0.5, 0.5, 0.5)$ point to the conduction band of several high-symmetry points are indicated by the arrows. The conduction band minimum (CBM) is also located at the $\mathbf{R}$ point. In Fig. S5 we show the temperature dependence of these band gaps, calculated using the AHC theory with a $20 \times 20 \times 20$ BZ sampling. The different changes with temperature exhibited by the different gaps indicate that temperature does not only change the absolute value of the band gaps, but also changes the shape of the band structure. Fig. S5 also shows the temperature dependence of the individual eigenvalues at the valence and conduction bands at several high-symmetry points in the vibrational BZ. For the minimum band gap at $\mathbf{R}$ discussed in the main text, the VBM decreases with increasing temperature, and the CBM increases with increasing temperature.

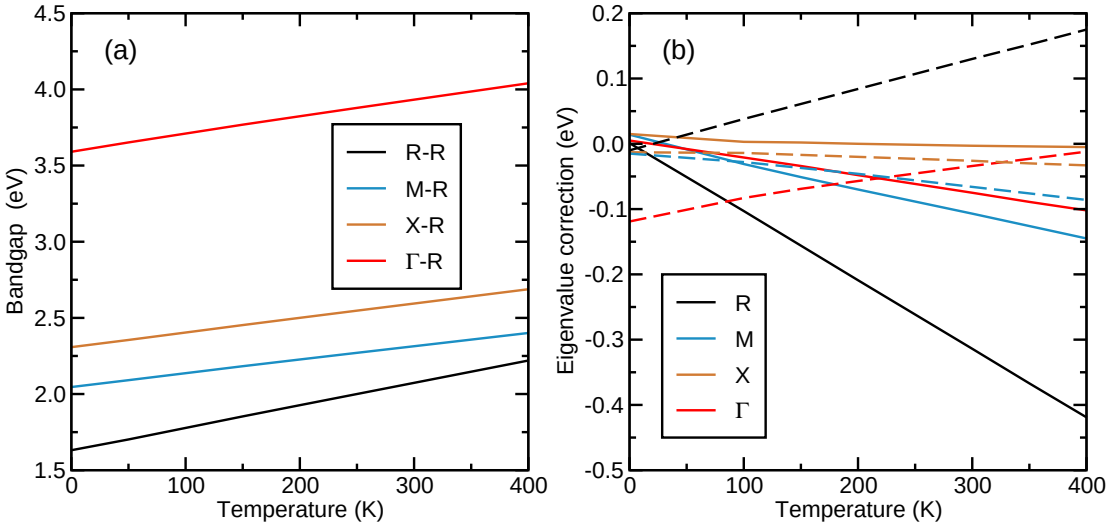

FIG. S5. (a) Temperature dependence of band gaps of $MAPbI_3$ from the VBM at the **R** point to the conduction band of several high-symmetry points in the BZ. (b) Temperature dependence of the individual eigenvalues at the valence (solid lines) and conduction (dashed lines) band at several high-symmetry points of the BZ. All calculations have been performed using the PBE functional and the AHC theory. The SOC and thermal expansion are not included.

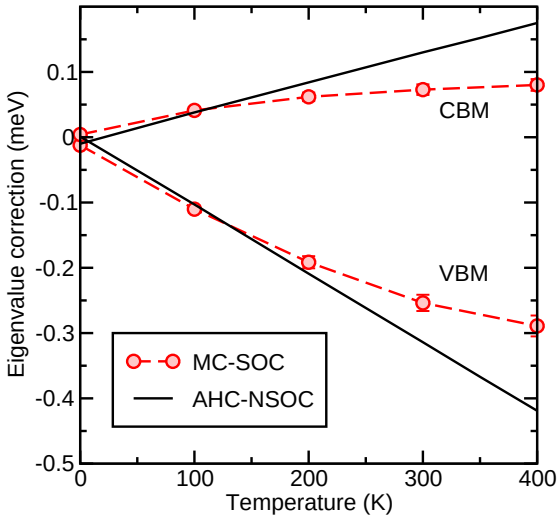

FIG. S6. Temperature dependence of the individual eigenvalues at the valence (lower lines) and conduction (upper lines) band at the **R**-point of the BZ. The calculations have been performed using the same numerical parameters as those in Fig. 3 of the main manuscript, but without the inclusion of thermal expansion.

In Fig. S6 we show the temperature dependence of the VBM and CBM at the **R** point using MC sampling with the PBE+SOC method, and a supercell of size $3 \times 3 \times 3$, numerical parameters corresponding to the final results presented in the main manuscript. For comparison, we also repeat the results arising from using the AHC theory. These calculations do not include the effects of thermal expansion, as a proper treatment of the average electrostatic potential in simulation cells of varying volumes would be required, but this is beyond the scope of the present work. The results in Fig. S6 show that the use of MC sampling corrects to a large extent the defficiencies of the AHC approach, by almost removing the temperature dependence of the CBM at temperatures above 290 K, of experimental interest. The results in Ref. [S15] suggest that the inclusion of thermal expansion would make the temperature dependence of the CBM negative, in agreement with the experimental observations.

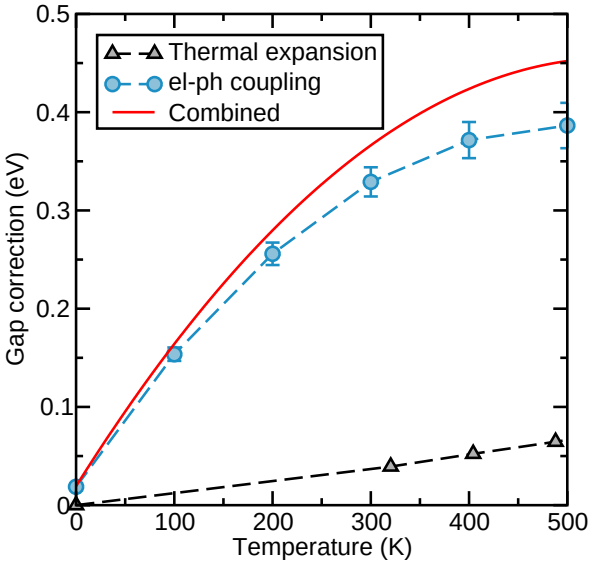

FIG. S7. Temperature dependence of the band gap of $MAPbI_3$ evaluated using thermal expansion only (black triangles), electron-phonon coupling only with MC and SOC on a $3 \times 3 \times 3$ supercell (blue circles), and both (red dashed-dotted line). The statistical error bars are included in all MC data points, although they are not visible in some as their size is smaller than the symbol size.

THERMAL EXPANSION

We study thermal expansion within the quasiharmonic approximation. The Helmholtz free energy of a solid at temperature T can be written as

$$\mathcal{F}(V,T) = \mathcal{U}(V,T) + E_{\rm vib}(V,T), \tag{S9}$$

where V is the volume, $\mathcal{U}$ is the electronic energy, and $E_{\rm vib}$ represent the vibrational energy. For systems with a band gap, $\mathcal{U}(V,T) \approx \mathcal{U}(V)$. The equilibrium volume at temperature T is determined by minimizing $\mathcal{F}(V,T)$, which we do by calculating the vibrational energy within the harmonic approximation at a range of volumes and then directly minimizing $\mathcal{F}(V,T)$.

The calculations have been performed using density functional theory (DFT) together with the Tkatchenko-Scheffler van der Waals scheme [S73]. Using this approach, we find that the lattice constant at zero temperature of 6.37 Åincreases to 6.40 Åat 300 K, which is in good agreement with experiment.[S56]

The change in the band gap due to thermal expansion is shown in Fig. S7, where it is compared with the electron-phonon coupling induced change. Electron-phonon coupling makes the largest contribution, with a band gap opening of about 0.40 eV at 500 K, compared to 0.07 eV for thermal expansion.

$CsPbI_3$

In Fig. S8 we show the temperature dependence of the band gap of $CsPbI_3$ evaluated using the quadratic approximation within the FD approach, and also using MC sampling. The calculations correspond to a sampling of the BZ with a grid of size $2\times2\times2$ and do not include SOC. As observed for $MAPbI_3$ in the main manuscript, high-order terms in the electron-phonon coupling are also necessary to accurately describe the temperature dependence of $CsPbI_3$.

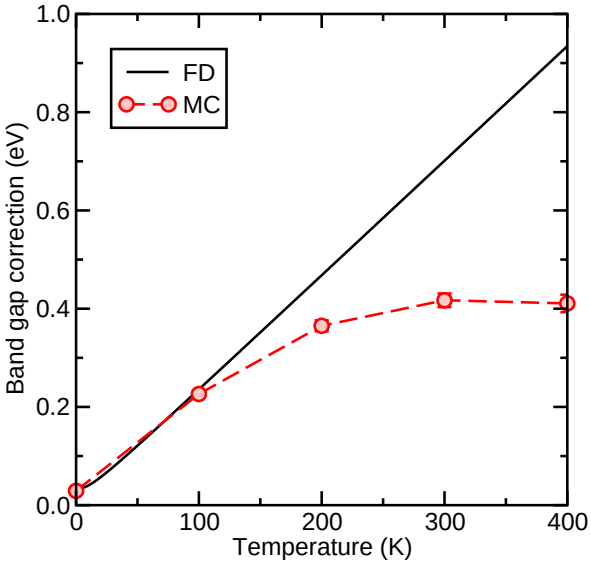

FIG. S8. Temperature dependence of the band gap of $CsPbI_3$ evaluated using the FD and MC methods. The calculations have been performed using the PBE functional, with a $2 \times 2 \times 2$ BZ grid, and without including SOC. Statistical error bars are included in the MC data points, but they are not visible for some data points as they are smaller than the symbols.